Article type: Full Paper

Manipulating picosecond photoresponse in van der Waals heterostructure photodetectors

Zhouxiaosong Zeng, Cuihuan Ge, Kai Braun, Martin Eberle, Yufan Wang, Biyuan Zheng, Chenguang Zhu, Xingxia Sun, Lanyu Huang, Ziyu Luo, Ying Chen, Huigao Duan, Shuangyin Wang, Dong Li, Fei Gao, Anlian Pan, Xiao Wang**

Prof. X. Wang, Dr. Z. Zeng, C. Ge, Y, Wang, L, Huang

School of Physics and Electronics, Hunan University, Changsha 410082, China

Dr. K. Braun, M. Eberle

Institute of Physical and Theoretical Chemistry and LISA+, University of Tübingen, Auf der Morgenstelle 18, 72076, Tübingen, Germany

Prof. A. Pan, Dr. B. Zheng, C. Zhu, X. Sun, Z. Luo, Y, Chen, Prof. D. Li

Key Laboratory for Micro-Nano Physics and Technology of Hunan Province, College of Materials Science and Engineering, Hunan University, Changsha, 410082, China

Prof. H. Duan

State Key Laboratory of Advanced Design and Manufacturing for Vehicle Body College of Mechanical and Vehicle Engineering, Hunan University, Changsha, 410082, China

Prof. S. Wang

State Key Laboratory of Chem/Bio-Sensing and Chemometrics, College of Chemistry and Chemical Engineering, Hunan University, Changsha, 410082, China

Prof. F. Gao

Department of Nuclear Engineering and Radiological Sciences, University of Michigan, Ann Arbor, Michigan, 48109, United States

E-mail: anlian.pan@hnu.edu.cn; xiao_wang@hnu.edu.cn

Keywords: time-resolved photocurrent, scanning photocurrent mapping, two-dimensional materials, van der Waals heterostructure, photodetector

Abstract: Self-powered ultrafast two-dimensional photodetectors have demonstrated great potential on imaging, sensing, and communication. Understanding the intrinsic ultrafast charge carrier generation and separation processes is essential for achieving high performance devices. However, probing and manipulating the ultrafast photoresponse are limited either by the temporal resolution of the conventional methods or the required sophisticated device configurations. Here, we construct van der Waals heterostructure photodetectors based on MoS_2/WSe_2 p-n and n-n junctions and manipulate the picosecond photoresponse by combining photovoltaic (PV) and photothermoelectric (PTE) effects. Taking time-resolved photocurrent (TRPC) measurements, we observe a TRPC peak at zero time delay with decay time down to 4 ps in the n-n junction device, in contrast to the TRPC dip in the p-n junction and pure WSe_2 devices, indicating an opposite current polarity between PV and PTE. More importantly, with an ultrafast photocurrents modulation, we realize a transition from a TRPC peak to a TRPC dip, and a detailed carrier transport dynamics is analyzed. Our study provides a deeper understanding of the ultrafast photocurrent generation mechanism in van der Waals heterostructures and offers a new perspective in instruction for designing more efficient self-powered photodetectors.

1. Introduction

Photodetectors based on two-dimensional (2D) semiconductors have attracted tremendous research interest because of the broadband photodetection from ultraviolet to the infrared region,[1-3] the picosecond intrinsic response speed,[4,5] and the integration of modern silicon technology.[6-8] The construction of 2D van der Waals heterostructure[9-12] realizes the high-frequency device applications up to tens of gigahertz, [13] which provides a potential to outperform the traditional technologies.[14,15] Moreover, self-powered photodetectors[16-20] without an external bias are highly

desirable in various fields for their low energy consumption and environmental-friendliness. Currently, state-of-the-art self-powered photodetectors are mainly based on the pure photovoltaic (PV) [21-24] or photothermoelectric (PTE) [18,25] effect, in which photogenerated charge carriers are separated either via built-in electric field or temperature gradient. Though, with conventional electrical transport measurements such as transfer and output characteristics or photoresponse measurements such as scanning photocurrent microscope (SPCM), the fundamental detection mechanisms of all these self-powered photodetectors have been investigated, the ultrafast time-solved charge carrier dynamic processes are concealed. Meanwhile, to maximumly utilize the photogenerated carriers and enhance detection performance, combining and manipulating different photodetection mechanisms need further differentiate respective charge carrier dynamics. Hence, understanding the contributions of both PV and PTE effects in one 2D material-based device with an ultrafast method is significant for more efficient high-frequency self-powered photodetector designs beyond state-of-the-art technique.

Time-resolved photocurrent (TRPC) technique combing pump-probe excitation configuration and photocurrent detection in the micro area has been demonstrated as an effective method in measuring the intrinsic response speed of electric devices. Previous researches have shown that 2D semiconductors, owning to their atomically thin thickness, can exhibit picosecond photocurrent change via PV effect,[4] PTE effect,[26] or photoconductive (PC) [27-29] effect. These photocurrent generation mechanisms individually display a TRPC dip at a small pump-probe delay, where probe beam-induced signal is suppressed because of the saturation in the ground state. With an increase in the delay time, due to the relaxation of excited carriers, a photocurrent recovery with the τ corresponding to the device response time is observed. Despite the extensive TRPC studies focused on the individual photocurrent generation mechanism, direct observation of their interaction and competition remains unexplored owning to the sophisticated device design and complicated carrier dynamics.

In this work, we demonstrated a comprehensive understanding of the interaction between PV and PTE effects on the picosecond time scale in MoS_2/WSe_2 heterostructure photodetectors. Using a TRPC setup, the ultrafast photoresponse in MoS_2/WSe_2 heterostructures with different WSe_2 thicknesses was investigated. Our results demonstrate an enhanced TRPC signal at zero time delay in MoS_2/1L WSe_2 n-n junctions with the decay time down to 4 ps, which is distinct to the phenomenon in the MoS_2/25 nm WSe_2 p-n junctions and in other previously reported devices tested by the same technique showing a conventional dip. Pump power-dependent and polarization-dependent photocurrent measurements indicate this enhanced TRPC signal is derived from the superposition between the PV and PTE currents in opposite directions. Further tuning the electrical field in the heterostructure by the external bias allows us to observe the TRPC transition from a peak to a dip and disentangle the two different dynamic processes.

2. Results and Discussion

2.1. Construction of heterostructures with different carrier types

TRPC signals could be distinct when a heterostructure photodetector operates at two different current generation mechanisms with different response times (τ_1, τ_2) (**Figure 1**a). Under illumination, a PV current from heterostructure is directly generated by the separation of charged photocarriers at the built-in electric field in the depletion region (Figure 1b). While an unbalanced lattice temperature distribution induced by the Seebeck coefficient difference between the two semiconductors creates a photo-thermal voltage, driving a PTE current in the whole device (Figure 1c). With the same or the opposite photocurrent polarity, the resulting TRPC signal from the superposition between PV and PTE current may no longer be a dip at zero time delay. To this end, we design different MoS_2/WSe_2 vertical heterostructure devices with different WSe_2 thicknesses (Figure 1d). We expect a transition from p-n to n-n junctions with the decrease in WSe_2 thickness, because the lattice deformation induced increase of selenium vacancies in thinner WSe_2 can lead to

the change in its doping concentration.[30] Here, two representative devices of MoS_2/25 nm WSe_2 and MoS_2/1L WSe_2 were compared in their electrical transport characteristics. The MoS_2/25 nm WSe_2 device displays a prominent rectifying behavior with a rectification ratio over 10^4 at negative gate voltages (Figure 1e), which is due to the integration of an ambipolar multilayer WSe_2 on the high electron-doped monolayer MoS_2 (Figure S1a and S1b, Supporting Information), indicating the formation of a p-n diode. In contrast, with the preferential-n-type monolayer WSe_2 (Figure S1c, Supporting Information), the MoS_2/1L WSe_2 heterostructure exhibits an n-n diode property at various gate voltages with the maximum rectification ratio approximate to 50 (Figure 1f).

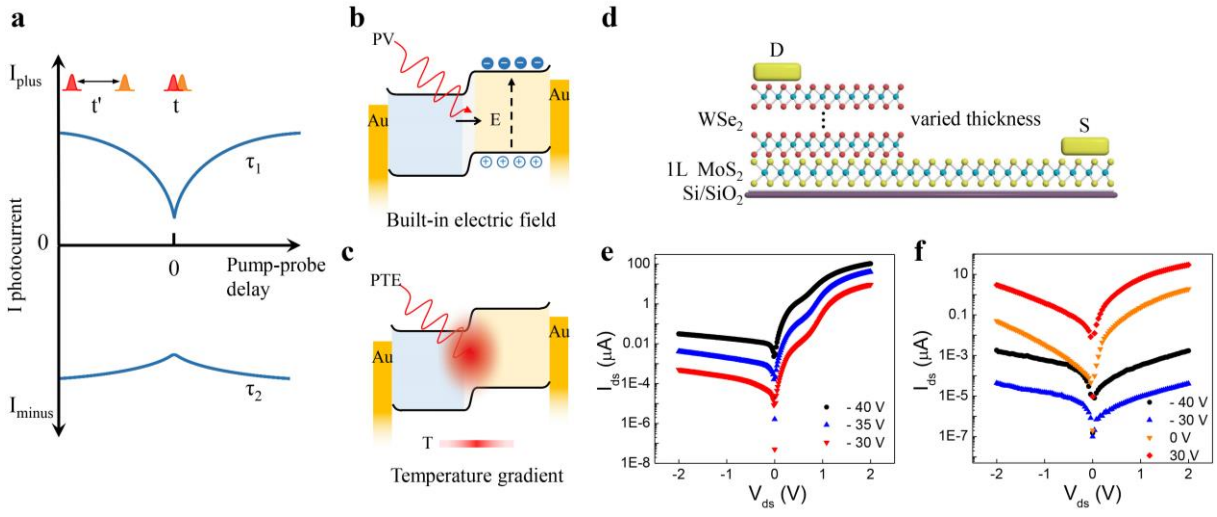

Figure 1. a) Schematic illustration of the simultaneously generated TRPC signal by different photocurrent generation mechanisms. b) Schematic illustration of the photovoltaic effect in the heterostructure. c) Schematic illustration of the photothermoelectric effect in the heterostructure. d) Schematic illustration of the MoS_2/WSe_2 vertical device with different WSe_2 thicknesses. e) I_{ds}-V_{ds} output characteristic curve in 1L MoS_2/25 nm WSe_2 p-n junction device at different gate voltages, showing the rectification ratio up to 2×10^4. f) I_{ds}-V_{ds} output characteristic curve in 1L MoS_2/1L WSe_2 n-n junction device at different gate voltages, showing the rectification ratio approximate to 50. V_{ds} refers to the bias on the WSe_2 and a $V_{ds} > 0$ corresponds to a forward bias, while the MoS_2 electrode was grounded.

2.2. TRPC dip in MoS_2/WSe_2 p-n junction

The spatially resolved photocurrent response (see Experimental Section) of the MoS_2/25 nm WSe_2 p-n junction device was characterized by a home-built SPCM at zero source-drain bias under the excitation of a pulsed 780 nm laser. Under 0 V gate voltage, a relatively weak photocurrent appears at the WSe_2 flake (Figure 2b), which is attributed to its larger light absorption and diffusion length compared with monolayer MoS_2. In contrast, the photocurrent maximum was obtained at the MoS_2/WSe_2 junction under the gate voltage of -40 V (Figure 2c), where the photogenerated carriers spontaneously separate with a higher efficiency, indicating that the photocurrent originates from the p-n junction rather than from the Schottky barriers at respective electrodes.[31,32] Meanwhile, the intensity of this photocurrent in the p-n junction is approximately one order of magnitude larger than the current intensity at 0 V gate voltage under the same excitation power (10 μW), indicating that the photocurrent is mainly derived from the PV effect. We further examined the response time of this vertical p-n junction device by our home-built TRPC setup (see Experimental Section). With the excitation of the pure probe beam, the photocurrent in MoS_2/WSe_2 device exhibits a typical sublinear power dependence (Figure 2d), which can be fitted to the power-law $I_{pc} \approx P^{0.5}$, where I_{pc} is the generated current intensity and P is the excitation power. With the existence of a pump beam, a suppressed photocurrent at zero time delay with the respect to the pump power further indicates the saturation of the photocurrent. Then the TRPC measurements of the MoS_2/WSe_2 photodetector under typical gate voltages were conducted compared with the pure 25 nm WSe_2 photodetector. All signals display a photocurrent dip at the small pump-probe delay with the different recovery rates. Hence, we extract the response time τ using the equation:

$$\frac{PC(\Delta t)}{PC(\Delta t \to \infty)} = 1 - A\exp(-\frac{\Delta t}{\tau}),$$

where the amplitude *A*, and time constant τ are the fitting parameters. The results yield the slowest response speed of 426 ps in pure 25 nm WSe_2 photodetector (black curve in Figure 2f), while approximate 25 fold and 50 fold enhancements were observed in heterostructure under 0 V (blue curve in Figure 2f) and -40V (red curve in Figure 2f) gate voltages, which is attributed to the more effective carrier separation and extraction by the type-II heterostructure[33,34] and p-n junction.[31,35] Thus far, the significant role of the PV effect in the p-n junction is apparent, while the participation of the PTE effect is hard to extract because of its same polarity and relatively small contribution with the PV current.

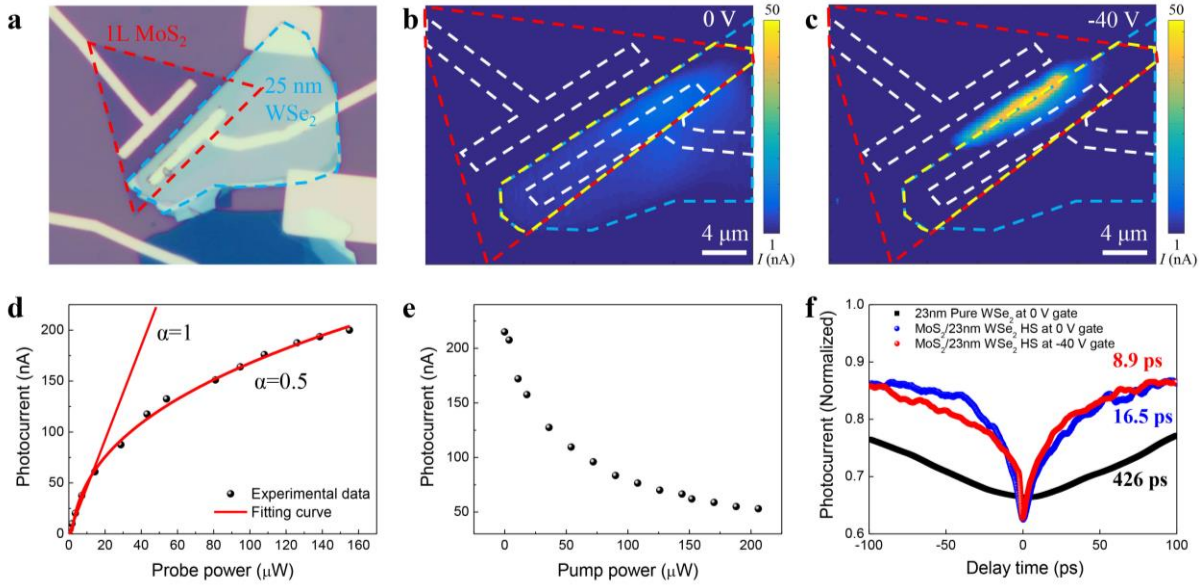

Figure 2. a) Optical image of the 1L MoS_2/25 nm WSe_2 heterostructure photodetector. Dashed lines highlight the CVD-grown MoS_2 (red) and exfoliated WSe_2 (blue). b) and c) Scanning photocurrent microscope (SPCM) images obtained at the gate voltages of 0 V and -40 V with an excitation wavelength of 780 nm and V_{ds}= 0 V, where the white, red and blue dashed lines indicate the locations of the electrodes, CVD-grown MoS_2 flake, and exfoliated WSe_2 flake, respectively. The photocurrent is mainly generated at the heterostructure region when the p-n junction is formed. d) Photocurrent as a function of probe power P with no pump. The lines are the power-law fits with I_{pc}

$\approx P^1$ and $I_{pc} \approx P^{0.5}$. e) Probe induced photocurrent as a function of pump power at 0 ps delay time. f) Time-resolved photocurrent measurements in pure 25 nm WSe_2 at V_g = 0 V (black) , MoS_2/25 nm WSe_2 heterostructure at V_g = 0 V (blue) and at V_g = -40 V (red), where an approximately 50 times faster response is obtained in p-n junction compared to the pure material.

2.3. TRPC peak in MoS_2/WSe_2 n-n junction

Considering the polarity of the PTE current could be influenced by the carrier type[36-38] in heterostructures, we further investigated the MoS_2/1L WSe_2 n-n junction photodetectors. In SPCM measurements, compared with the p-n junction device, the photocurrent map demonstrates a similar photocurrent maximum appearing at the n-n junction, but with the decrease in WSe_2 thickness, the generated photocurrent was approaching the electrode (Figure 3b). This phenomenon could be an indication that the PTE effect contributed more photocurrent, and therefore we performed the TRPC studies. An obviously enhanced peak signal at zero pump-probe time delay was observed with the response time approximate to 4 ps (Figure 3c), which is distinct to the previously reported phenomenon in transition metal dichalcogenides (TMDCs)[4,28] and their heterostructures[27,29,39-41] by the same measurement technique. Meanwhile, the above phenomenon can be observed in another MoS_2/4 nm WSe_2 n-n junction device (Figure 3d-f) with a little slowed response time to 8 ps, which can be explained as the increased out-of-plane drift time in thicker devices according to the transient time expression of $\tau_{tran} = L^2/\mu V_{bias}$.[41]

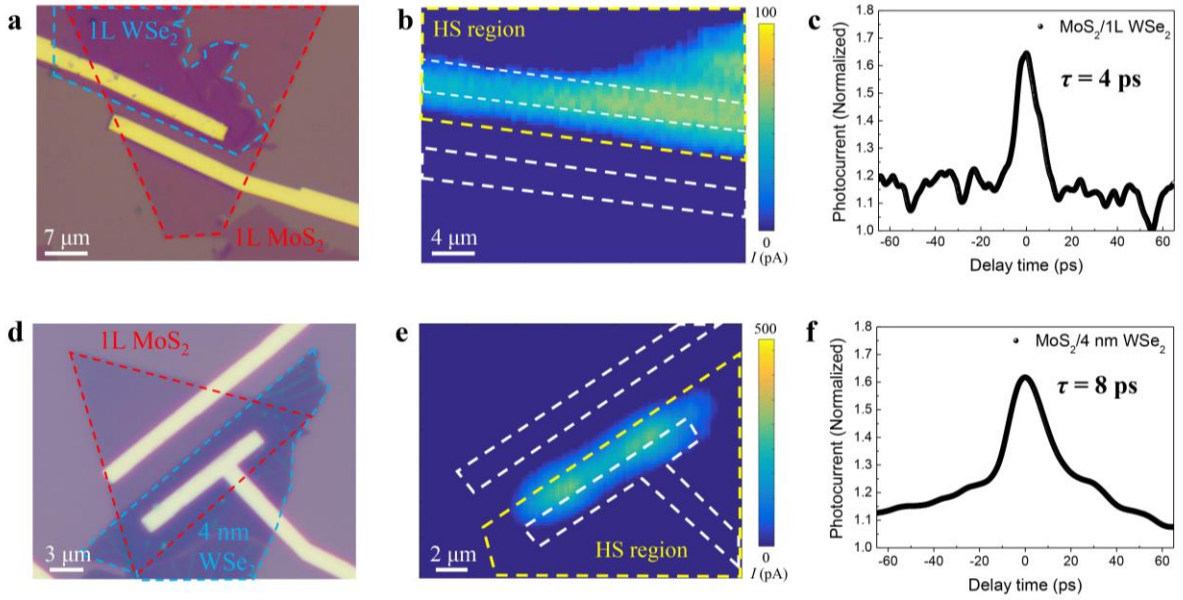

Figure 3. a) and d) Optical images of the MoS_2/1L WSe_2 heterostructure photodetector and MoS_2/4 nm WSe_2 heterostructure photodetector. b) and e) Corresponding SPCM images obtained with the excitation wavelength of 780 nm on the devices in (a) and (d) with the V_{ds} = 0 V and V_g = 0V, where the white and yellow dashed lines indicate the locations of the electrodes and heterostructure region, respectively. The obtained photocurrent gets closer to the electrode with the decrease of WSe_2 thickness. c) and f) TRPC measurements corresponding to the devices in (a) and (d), where ultrafast positive signals are obtained at zero delay time.

To elucidate these unique signals, we further performed pump power and polarization-dependent photocurrent measurements. In TRPC experiments, with the increase in pump power, an enhanced photocurrent signal at zero time delay gradually appeared (**Figure 4**a), while the photocurrent background was suppressed. We extracted the photocurrent changes at the background and at the peak in absolute value, where a linearly increased photocurrent enhancement at zero time delay and a linearly decreased photocurrent background with the increase in pump power were shown (Figure 4b). Besides, photocurrent polarization could distinguish different photocurrent generation

mechanisms because of different plasmonic hot carrier injection efficiencies from a metal electrode to a semiconductor.[42] Here, the enhanced photocurrent peak in MoS_2/1L WSe_2 n-n junction was anisotropic and had an anisotropy ratio of 1.63 (Figure S7e, Supporting Information), which was between the anisotropy ratios of 1.1 in PV response and 4.25 in PTE response in our study on the pure MoS_2 (Figure S7b and S7c, Supporting Information)." While no clear plasmonic effect induced photocurrent enhancement similar to the previous works[43,44] was observed, possibly because the input electric field is difficult to be confined with the channel width of 5 to 7 μm in our case. The results in power-dependent and polarization-dependent TRPC both indicate that the TRPC peak could arise from the combined photocurrent in both PV and PTE effects. Considering the generated photocurrent can be easily modulated by the external bias for a relatively weak built-in electric field in n-n junction, we further conducted TRPC measurements with different drain voltages. When applied bias was in the same direction as the built-in electric field (V_{ds} < 0 V), an increased TRPC signal and an almost unchanged peak proportion were found with the increase in drain voltages, demonstrating only the photocurrent intensity has changed. Whereas varying the junction from reverse bias to forward bias (V_{ds} > 0 V), a TRPC signal transition from a peak to a dip at zero time delay was observed at V_{ds} = 0.6 V (Figure 4c), and this phenomenon appeared more prominent with larger bias.

2.4. Analysis of PV and PTE effects

As the TPRC signal can be modulated from the distinct peak to the normal dip under the external bias, we consider that the PV and PTE effects contribute a photocurrent with opposite polarities in the MoS_2/WSe_2 n-n junction at the V_{ds} = 0. Under the 780 nm laser excitation, the absorption of the WSe_2 layer generates electron-hole pairs which are separated by the built-in electrical field at the junction, contributing the negative PV current (blue arrow process in Figure 4d). Meanwhile, a local heating created by the laser illumination is converted into a voltage difference across the junction,

which produces a PTE current. In a traditional metal-semiconductor-metal (MSM) structure, taking n-type materials as an example, the illumination near the contact leads to the electron concentration increase and a tilt of energy band, where excessive electrons diffuse to another cold contact contributing to a PTE current with the same polarity of PV current.[45,46] Whereas in our case, the temperature increase at the MoS_2/WSe_2 junction induces a competition of the PTE current flow by these two materials depending on the Seebeck coefficient difference between them. Previous reports demonstrate that the monolayer TMDCs exhibit similar thermoelectric properties with a comparable intrinsic Seebeck coefficient.[47,48] However, thermopower can be influenced by the charge carrier density and the Seebeck coefficient will monotonously increase with the decrease in carrier doping concentration,[46,49] according to the Mott formula. Hence compared with highly-doped MoS_2, the lowly doped WSe_2 has a larger Seebeck coefficient and the diffusion of its electrons to the drain contact dominates the polarity of PTE current (red arrow process in Figure 4d), contributing an opposite effect to the PV current. In this situation, the temperature difference induced voltage also reduces the barrier between MoS_2 and WSe_2, making the generation of PTE current easier.

On the temporal scale, the PV effect in our MoS_2/WSe_2 n-n junction leads to a response time of several picoseconds because of the short carrier lifetime in thin-layered TMDCs[4,50] and their heterostructures.[27] While an almost unchanged TRPC was obtained by the pure PTE effect in the 1L MoS_2 device (Figure S9c), which is attributed to the longstanding cooling time of excited hot carriers through the slow coupling to acoustic phonons. Hence, we propose that with the pure probe excitation, the PV (red area in Figure 4e) and PET (dark blue area in Figure 4e) current first has an opposite polarity, and with the existence of pump beam, an incompletely offset photocurrent by the opposite PV and PTE effects is achieved in small pump-probe delay (the superposition of orange and light blue area in Figure 4e upper plane), contributing a relatively large net photocurrent. With the increase in delay time, the suppressed PV current quickly recovered, while the PTE current stay

invariant for a longer hot carrier relaxation time. Therefore, the recovered PV current induces a larger photocurrent offset and the whole photocurrent is reduced at the large pump-probe delay (the superposition of orange and light blue area in Figure 4e lower plane).

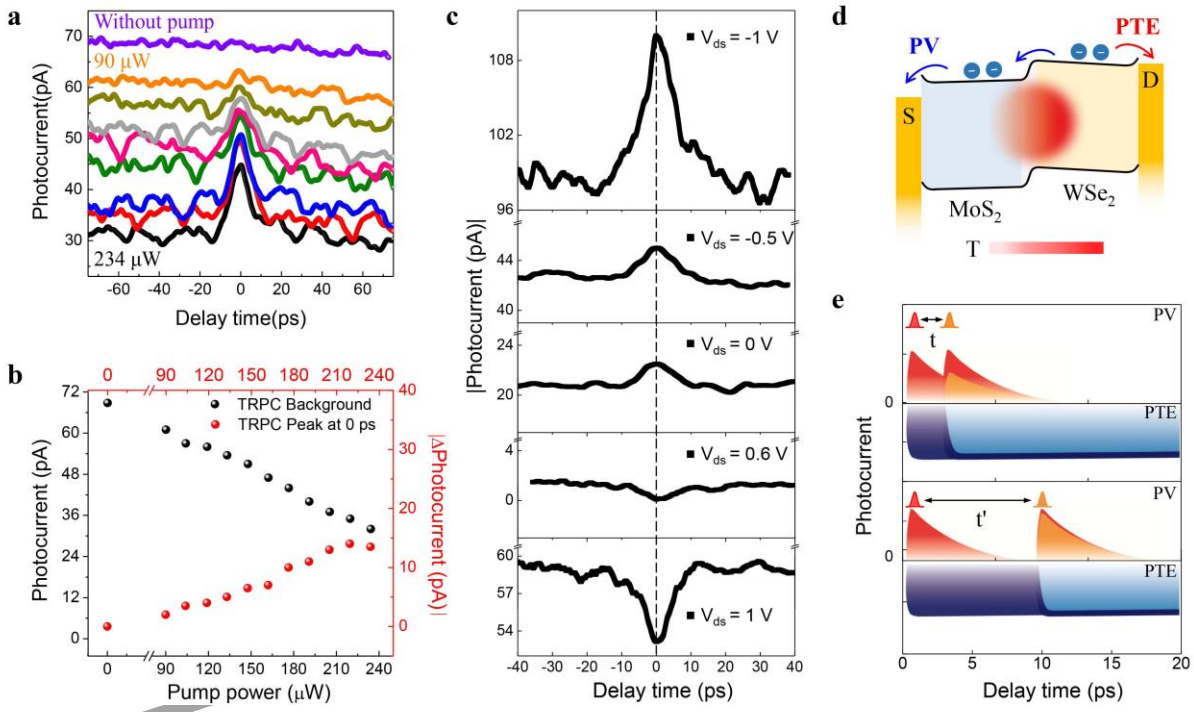

Figure 4. a) TRPC measurements at different pump powers. b) Extracted background photocurrent (black) and the |ΔPC| (red) change with the increase of pump power. The background photocurrent is defined as the photocurrent with the pump-probe delay t → ∞, while the |ΔPC| is defined as the difference between the photocurrent (t = 0) and photocurrent (t → ∞). c) TRPC measurements with different V_{ds} biases applied at WSe_2 electrode. When the V_{ds} is reverse biased, an enhanced signal is obtained at the 0 ps time delay. When the V_{ds} is forward biased, a suppressed signal is obtained at the 0 ps time delay. d) Schematic illustration of the opposite PV and PTE current generation in one device after pulsed laser illumination, where the blue arrows indicate the generation of negative PV current by the build-in electric field while the red arrow indicates the WSe_2 dominant positive PTE current due to its larger Seebeck coefficient. e) Schematic illustration of the photocurrent superposition between PV and PTE effect in MoS_2/WSe_2 n-n junction photodetector. Here the PV

(PTE) current in the red (dark blue) area is induced by the individual pump or probe excitation, while the PV (PTE) current in the orange (light blue) area is induced by the probe excitation with the pump.

3. Conclusion

In summary, using time-resolved photocurrent measurements in combination of scanning photocurrent microscope, we provided a comprehensive picture of tangled PTE effect with the PV effect in generation of photocurrent on the picosecond time scale. The carrier type change in MoS_2/WSe_2 junction photodetector with different WSe_2 thicknesses determined the PV and PTE current polarity. An enhanced TRPC signal at zero pump-probe delay in MoS_2/1L WSe_2 n-n junction contrast to the dip in MoS_2/25 nm WSe_2 p-n junction reflected an opposite polarity of PV and PTE current, which can be further modulated by the external bias. The deeper understanding of PV and PTE mechanisms in van der Waals heterostructures can be an instruction for designing more efficient photodetectors.

4. Experimental Section

Sample preparation and device fabrication: MoS_2/WSe_2 vertical heterostructure devices with different thicknesses were fabricated via transferring mechanically exfoliated WSe_2 onto the chemical vapor deposition (CVD) synthesized monolayer MoS_2. In preparation of MoS_2 samples, the powders of sulfur and MoO_3 in two ceramic boats were placed in the upstream side and the center of the furnace, respectively. A cleaned silicon substrate with a 300 nm-thick silicon dioxide layer was face-down mounted on the MoO_3 boat. The furnace temperature was ramped up to 780 °C and kept at that temperature for 10 min with an Ar gas flow rate of 150 standard cubic centimeter per minute (sccm). After that, the furnace was cooled to room temperature naturally. Then a WSe_2 flake mechanically exfoliated onto transparent polydimethylsiloxane (PDMS) was aligned and transferred onto the synthesized MoS_2 flake with the help of a microscope. Cr/Au (10 nm/50 nm) conducting electrodes on top of MoS_2/WSe_2 heterostructures with a channel length of 5 to 7 μm were fabricated using standard electron beam lithography (EBL), metal thermal evaporation, and lift-off processes.

Basic characterization: Atomic force microscopy (AFM) (Bruker Dimension Icon) in the tapping mode was used to identify the thickness of the samples. Raman, photoluminescence, and TRPL (Time-resolved photoluminescence) measurements of the samples were taken using a confocal microscope (WITec, alpha-300) equipped with a 50× objective lens (Zeiss EC Epiplan). The excitation source of the Raman and PL spectra was a 532 nm continuous-wave laser, and the laser beam was focused to 1 μm on the samples. The TRPL measurements of the samples were detected with a streak camera system (Hamamatsu, C10910) using laser pulses at 400 nm (repetition rate of 80 MHz, pulse width of 100 fs) as the excitation source. The electrical properties were measured with an Agilent-B1500 semiconductor analyzer in a LakeShore vacuum chamber of 10^{-4} Pa.

SPCM and TRPC measurements: Scanning photocurrent microscopy (SPCM) and time-resolved photocurrent measurements (TRPC) were performed on our home-built setup. In SPCM measurements, a 780 nm fiber laser (NPI Rainbow 780 OEM) with a pulse width of 80 fs and a 488 nm continuous wave laser were chopped by a mechanical chopper at 1050 Hz, and then focused onto the sample by a long working distance objective (Olympus LMPLFLN 50×) near the diffraction limit. The generated photocurrent was collected by a lock-in amplifier (Stanford SR830) at the chopped frequency with a background noise of approximately 0.2 pA. The SPCM measurements with the resolution close to the diffraction limit were performed by raster scanning the entire device mounted on a piezoelectric translation stage (Piezoconcept LT3) according to the fixed laser spot. In TRPC studies, a 780 nm pulse laser was split into two independent beams to form a pump-probe measurement configuration, and the probe beam was chopped so that the lock-in amplifier could only measure its photocurrent. The pump beam was delayed by different path lengths, with the delay time precisely controlled by a mechanical delay stage (Thorlabs DDSM100/M). The pump and probe beams were recombined by a beam splitter after the delay line stage, and focused onto the sample using the same long working distance objective. The temporal resolution of the TRPC set-up is about 1 ps. A gate voltage was applied by a Source Measure Unit (Keithley 2400) in gate-dependent SPCM and TRPC measurements.

Supporting Information

Supporting Information is available from the Wiley Online Library or from the author.

Acknowledgements

Z. Zeng and C. Ge contributed equally to this work. This work was supported by the National Natural Science Foundation of China (Nos. 52022029, 91850116, 51772084, U19A2090), the Sino-German

Center for Research Promotion (No. GZ1390), and the Hunan Provincial Natural Science Foundation of China (No. 2018RS3051, 2019XK2001).

Received: ((will be filled in by the editorial staff))
Revised: ((will be filled in by the editorial staff))
Published online: ((will be filled in by the editorial staff))

References

[1] Q. X. Qiu, Z. M. Huang, *Adv. Mater.* **2021**, *33*, 2008126.

[2] F. N. Xia, H. Wang, D. Xiao, M. Dubey, A. Ramasubramaniam, *Nat. Photonics* **2014**, *8*, 899.

[3] C. Y. Liu, J. S. Guo, L. W. Yu, J. Li, M. Zhang, H. Li, Y. C. Shi, D. X. Dai, *Light Sci. Appl.* **2021**, *10*, 123.

[4] H. N. Wang, C. J. Zhang, W. M. Chan, S. Tiwari, F. Rana, *Nat. Commun.* **2015**, *6*, 8831.

[5] P. Ma, Y. Salamin, B. Baeuerle, A. Josten, W. Heni, A. Emboras, J. Leuthold, *ACS Photonics* **2019**, *6*, 154.

[6] F. H. L. Koppens, T. Mueller, P. Avouris, A. C. Ferrari, M. S. Vitiello, M. Polini, *Nat. Nanotechnol.* **2014**, *9*, 780.

[7] D. Akinwande, C. Huyghebaert, C. H. Wang, M. I. Serna, S. Goossens, L. J. Li, H. S. P. Wong, F. H. L. Koppens, *Nature* **2019**, *573*, 507.

[8] K. C. Zhu, C. Wen, A. A. Aljarb, F. Xue, X. M. Xu, V. Tung, X. X. Zhang, H. N. Alshareef, M. Lanza, *Nature Electronics* **2021**, *4*, 775.

[9] X. Zhou, X. Z. Hu, S. S. Zhou, H. Y. Song, Q. Zhang, L. J. Pi, L. Li, H. Q. Li, J. T. Lu, T. Y. Zhai, *Adv. Mater.* **2018**, *30*, 1703286.

[10] F. K. Wang, P. Luo, Y. Zhang, Y. Huang, Q. F. Zhang, Y. Li, T. Y. Zhai, *Science China-Materials* **2020**, *63*, 1537.

[11] F. K. Wang, J. Wu, Y. Zhang, S. J. Yang, N. Zhang, H. Q. Li, T. Y. Zhai, *Science China-Materials* **2022**, *65*, 451.

[12] L. X. Liu, T. Y. Zhai, *Infomat* **2021**, *3*, 3.

[13] N. Flory, P. Ma, Y. Salamin, A. Emboras, T. Taniguchi, K. Watanabe, J. Leuthold, L. Novotny, *Nat. Nanotechnol.* **2020**, *15*, 118.

[14] A. Rogalski, *Progress In Quantum Electronics* **2003**, *27*, 59.

[15] A. Rogalski, *Progress In Quantum Electronics* **2012**, *36*, 342.

[16] M. Buscema, J. O. Island, D. J. Groenendijk, S. I. Blanter, G. A. Steele, H. S. J. van der Zant, A. Castellanos-Gomez, *Chem. Soc. Rev.* **2015**, *44*, 3691.

[17] M. S. Long, P. Wang, H. H. Fang, W. D. Hu, *Adv. Funct. Mater.* **2019**, *29*, 1803807.

[18] X. W. Lu, L. Sun, P. Jiang, X. H. Bao, *Adv. Mater.* **2019**, *31*, 1902044.

[19] J. Fang, Z. Zhou, M. Xiao, Z. Lou, Z. Wei, G. Shen, *Infomat* **2020**, *2*, 291.

[20] M. Wu, Y. Xiao, Y. Zeng, Y. Zhou, X. Zeng, L. Zhang, W. Liao, *Infomat* **2021**, *3*, 362.

[21] F. Wu, Q. Li, P. Wang, H. Xia, Z. Wang, Y. Wang, M. Luo, L. Chen, F. S. Chen, J. S. Miao, X. S. Chen, W. Lu, C. X. Shan, A. L. Pan, X. Wu, W. C. Ren, D. Jariwala, W. D. Hu, *Nat. Commun.* **2019**, *10*, 4663.

[22] C. J. Zhou, S. Y. Zhang, Z. Lv, Z. C. Ma, C. Yu, Z. H. Feng, M. S. Chan, *npj 2d Mater. Appl.* **2020**, *4*, 46.

[23] X. K. Zhang, B. S. Liu, L. Gao, H. H. Yu, X. Z. Liu, J. L. Du, J. K. Xiao, Y. H. Liu, L. Gu, Q. L. Liao, Z. Kang, Z. Zhang, Y. Zhang, *Nat. Commun.* **2021**, *12*, 1522.

[24] S. Ghosh, A. Varghese, K. Thakar, S. Dhara, S. Lodha, *Nat. Commun.* **2021**, *12*, 3336.

[25] J. Liu, F. N. Xia, D. Xiao, F. J. G. de Abajo, D. Sun, *Nat. Mater.* **2020**, *19*, 830.

[26] D. Sun, G. Aivazian, A. M. Jones, J. S. Ross, W. Yao, D. Cobden, X. D. Xu, *Nat. Nanotechnol.* **2012**, *7*, 114.

[27] M. Massicotte, P. Schmidt, F. Vialla, K. G. Schadler, A. Reserbat-Plantey, K. Watanabe, T. Taniguchi, K. J. Tielrooij, F. H. L. Koppens, *Nat. Nanotechnol.* **2016**, *11*, 42.

[28] K. T. Vogt, S. F. Shi, F. Wang, M. W. Graham, *J. Phys. Chem. C* **2020**, *124*, 15195.

[29] M. Massicotte, P. Schmidt, F. Vialla, K. Watanabe, T. Taniguchi, K. J. Tielrooij, F. H. L. Koppens, *Nat. Commun.* **2016**, *7*, 12174.

[30] Z. Wang, H. Xia, P. Wang, X. H. Zhou, C. S. Liu, Q. H. Zhang, F. Wang, M. L. Huang, S. Y. Chen, P. S. Wu, Y. F. Chen, J. F. Ye, S. Y. Huang, H. G. Yan, L. Gu, J. S. Miao, T. X. Li, X. S. Chen, W. Lu, P. Zhou, W. D. Hu, *Adv. Mater.* **2021**, *33*, 2104942.

[31] R. Cheng, D. H. Li, H. L. Zhou, C. Wang, A. X. Yin, S. Jiang, Y. Liu, Y. Chen, Y. Huang, X. F. Duan, *Nano Lett.* **2014**, *14*, 5590.

[32] C. H. Lee, G. H. Lee, A. M. van der Zande, W. C. Chen, Y. L. Li, M. Y. Han, X. Cui, G. Arefe, C. Nuckolls, T. F. Heinz, J. Guo, J. Hone, P. Kim, *Nat. Nanotechnol.* **2014**, *9*, 676.

[33] H. M. Zhu, J. Wang, Z. Z. Gong, Y. D. Kim, J. Hone, X. Y. Zhu, *Nano Lett.* **2017**, *17*, 3591.

[34] F. Li, B. Y. Xu, W. Yang, Z. Y. Qi, C. Ma, Y. J. Wang, X. H. Zhang, Z. R. Luo, D. L. Liang, D. Li, Z. W. Li, A. L. Pan, *Nano Res.* **2020**, *13*, 1053.

[35] Y. Chen, X. D. Wang, L. Huang, X. T. Wang, W. Jiang, Z. Wang, P. Wang, B. M. Wu, T. Lin, H. Shen, Z. M. Wei, W. D. Hu, X. J. Meng, J. H. Chu, J. L. Wang, *Nat. Commun.* **2021**, *12*, 4030.

[36] N. M. Gabor, J. C. W. Song, Q. Ma, N. L. Nair, T. Taychatanapat, K. Watanabe, T. Taniguchi, L. S. Levitov, P. Jarillo-Herrero, *Science* **2011**, *334*, 648.

[37] J. C. W. Song, M. S. Rudner, C. M. Marcus, L. S. Levitov, *Nano Lett.* **2011**, *11*, 4688.

[38] J. Zhang, H. J. Liu, L. Cheng, J. Wei, J. H. Liang, D. D. Fan, P. H. Jiang, L. Sun, J. Shi, *J. Mater. Chem. C* **2016**, *4*, 991.

[39] M. Massicotte, F. Vialla, P. Schmidt, M. B. Lundeberg, S. Latini, S. Haastrup, M. Danovich, D. Davydovskaya, K. Watanabe, T. Taniguchi, V. I. Fal'ko, K. S. Thygesen, T. G. Pedersen, F. H. L. Koppens, *Nat. Commun.* **2018**, *9*, 1633.

[40] Y. C. Kim, V. T. Nguyen, S. Lee, J. Y. Park, Y. H. Ahn, *ACS Appl. Mater. Interfaces* **2018**, *10*, 5771.

[41] Z. Zeng, K. Braun, C. Ge, M. Eberle, C. Zhu, X. Sun, X. Yang, J. Yi, D. Liang, Y. Wang, L. Huang, Z. Luo, D. Li, A. Pan, X. Wang, *(Preprint) Fundam. Res.*, https://doi.org/10.1016/j.fmre.2021.09.018, 9 **2021**.

[42] T. Hong, B. Chamlagain, S. R. Hu, S. M. Weiss, Z. X. Zhou, Y. Q. Xu, *ACS Nano* **2015**, *9*, 5357.

[43] J. R. Fang, D. Wang, C. T. DeVault, T. F. Chung, Y. P. Chen, A. Boltasseva, V. M. Shalaev, A. V. Kildishev, *Nano Lett.* **2017**, *17*, 57.

[44] Y. L. Guo, L. W. Guo, K. Y. Zhou, J. W. Yang, Z. Xu, X. D. Bai, *Aip Advances* **2021**, *11*, 085124.

[45] M. Buscema, M. Barkelid, V. Zwiller, H. S. J. van der Zant, G. A. Steele, A. Castellanos-Gomez, *Nano Lett.* **2013**, *13*, 358.

[46] C. C. Wu, D. Jariwala, V. K. Sangwan, T. J. Marks, M. C. Hersam, L. J. Lauhon, *J. Phys. Chem. Lett.* **2013**, *4*, 2508.

[47] D. L. Li, Y. N. Gong, Y. X. Chen, J. M. Lin, Q. Khan, Y. P. Zhang, Y. Li, H. Zhang, H. P. Xie, *Nano-Micro Lett.* **2020**, *12*, 36.

[48] D. Wickramaratne, F. Zahid, R. K. Lake, *J. Chem. Phys.* **2014**, *140*, 124710.

[49] J. Wu, H. Schmidt, K. K. Amara, X. F. Xu, G. Eda, B. Ozyilmaz, *Nano Lett.* **2014**, *14*, 2730.

[50] H. N. Wang, C. J. Zhang, F. Rana, *Nano Lett.* **2015**, *15*, 8204.

The table of contents:

Comprehensive understanding of interaction and competition between photovoltaic and photothermoelectric effects is demonstrated via TRPC measurement technique. Compared to MoS_2/multilayer WSe_2 p-n junction having a conventional TRPC dip, MoS_2/1L WSe_2 n-n junction processes a distinct TRPC peak, which is attributed to the opposite polarity between photovoltaic and photothermoelectric currents and can be further modulated via an external bias.

Zhouxiaosong Zeng , Cuihuan Ge , Kai Braun, Martin Eberle, Yufan Wang, Biyuan Zheng, Chenguang Zhu, Xingxia Sun, Lanyu Huang, Ziyu Luo, Ying Chen, Huigao Duan, Shuangyin Wang, Dong Li, Fei Gao, Anlian Pan*, Xiao Wang *

Manipulating picosecond photoresponse in van der Waals heterostructure photodetectors

ToC figure